Upper–Lower Layer Coupling of Recurrent Circulation Patterns in the Gulf of Mexico

ERICK R. OLVERA-PRADO,[a] EFRAÍN MORELES,[b] JORGE ZAVALA-HIDALGO,[a] AND ROSARIO ROMERO-CENTENO[a]

[a] *Instituto de Ciencias de la Atmósfera y Cambio Climático, Universidad Nacional Autónoma de México, Coyoacán, Mexico City, Mexico*
[b] *Instituto de Ciencias del Mar y Limnología, Unidad Académica Procesos Oceánicos y Costeros, Universidad Nacional Autonoma de Mexico, Coyoacán, Mexico City, Mexico*

(Manuscript received 1 December 2021, in final form 12 October 2022)

ABSTRACT: The study of the relationship between the upper and lower layers in the Gulf of Mexico (GoM) has experienced a lot of progress in recent years. Nevertheless, an examination of their coupling for the entire GoM in a statistically consistent manner is still needed. Layer thickness data from a GoM 21-yr free-running simulation are used to examine the coupling between the upper (<250 m) and lower (>1000 m) layers, focusing on the dominant modes of variability through a Hilbert empirical orthogonal function (HEOF) analysis. The results show that the three leading modes are associated with the coupling between both layers during the life cycle of the Loop Current (LC) and the LC eddy (LCE) separation process, consistent with previous observational studies. These modes are cyclical, with periodicities in agreement with the mean LCE separation period, indicating recurrence of the circulation patterns. The fourth mode of the upper layer is associated with the translation of LCEs and their dissipation in the northwestern GoM, while in the lower layer it captures variability related to the strengthening of the circulation along the Sigsbee Gyre western branch. This mode does not show cyclicity, suggesting persistence of the associated circulation patterns with a dominant time scale of 14 months. Evidence and corroboration of recently observed lower-layer circulation features are provided. The application of the HEOF technique used here can complement the three-dimensional oceanic assimilation methods by projecting surface information to depth in a statistically consistent manner.

SIGNIFICANCE STATEMENT: The purpose of this study is to better understand the relationship between the upper and lower ocean layers in the Gulf of Mexico. While much is known about their variability separately, an examination of the coupling through the whole region and in a long time period is still needed. We use a free numerical simulation of the circulation in the Gulf to accomplish this goal. The dominant circulation patterns in the lower layer are tied to the upper ones and are governed by the same temporal scales. Our findings point to a way to better understand the response of deep circulation to upper circulation, and may contribute to a better prediction of ocean dynamics.

KEYWORDS: Abyssal circulation; Bottom currents; Eddies; Ocean circulation; Empirical orthogonal functions; Ocean models

1. Introduction

The Gulf of Mexico (GoM) circulation behaves like a two-layer system with different circulation patterns in the upper layer, roughly above 1000-m depth, and the lower layer, below 1200-m depth (Hamilton 2009). There has been substantial progress in the understanding of the upper-layer circulation, which is characterized by being highly energetic and stratified, where the main circulation pattern is the Loop Current System (LCS) composed of the Loop Current (LC) and the Loop Current Eddies (LCEs) (Sturges and Leben 2000; Leben 2005; Zavala-Hidalgo et al. 2006; Vukovich 2007, 2012).

On the other hand, the historically less studied GoM lower-layer circulation is less energetic than the upper circulation, with nearly depth-independent circulation patterns. The first studies of the deep GoM were devoted to understanding and characterizing the currents around 2000 m depth and the dynamics of the topographic Rossby waves (TRWs) over the slope in the northern GoM (Hamilton 1990; Hamilton and Lugo-Fernandez 2001; Hamilton 2007, 2009; Dukhovskoy et al. 2009; Morey and Dukhovskoy 2013). Recently, from a 4-yr observational study using subsurface floats and a dense array of moorings in the LC region, Hamilton et al. (2016) and Pérez-Brunius et al. (2018) described the large-scale circulation throughout the deep GoM and identified three dominant patterns, namely, a cyclonic boundary current in the entire deep GoM, a cyclonic gyre in the Sigsbee abyssal plain [the Sigsbee Abyssal Gyre (SAG)], and a very high eddy kinetic energy region in the eastern Gulf. Using a set of numerical models, Morey et al. (2020) found that these deep patterns are well simulated, despite some differences in their structure, strength, and variability, and concluded that the models have the necessary dynamics to realistically describe the deep-layer circulation.

Several observational and numerical studies have characterized the coupling between the upper and lower layers with

Supplemental information related to this paper is available at the Journals Online website: https://doi.org/10.1175/JPO-D-21-0281.s1.

Corresponding author: Erick R. Olvera-Prado, erick@atmosfera.unam.mx

DOI: 10.1175/JPO-D-21-0281.1

many approaches, focusing mainly on the eastern basin and over particular periods. Bunge et al. (2002) found a relationship between the observed deep transport in the Yucatan Chanel and the LC extension, a result that Nedbor-Gross et al. (2014) supported with a continuous 54-yr simulation of the GoM. Oey (2008) found that deep cyclones amplifying off the west Florida slope cause the LC to develop a "neck" and showed this process to be the LC's dominant mode of upper-to-deep variability. Chang and Oey (2011) found a relationship between the SAG circulation and the LC cycle. Donohue et al. (2016b) used a set of observational arrays covering the LC region and found that during the LCE detachment and formation events, a marked increase in deep eddy kinetic energy occurs coincident with the growth of a large-scale meander along the northern and eastern parts of the LC. The strong vertical phase tilt between the interacting upper and deep eddies, consistent with the development of baroclinic instability, eventually leads to the "necking down" of the LC that culminates in the separation of an LCE. An anticyclone–cyclone pair (modon) in the deep ocean that accompanies the LCE as it travels westward has been documented in several observational and numerical studies (Welsh and Inoue 2000; Lee and Mellor 2003; Romanou et al. 2004; Chérubin et al. 2005; Tenreiro et al. 2018). Furey et al. (2018) suggest that the disintegration of this deep modon, caused by the interaction with the northwestern continental slope, may lead to the enhancement of the SAG and the boundary current in the Bay of Campeche region. Maslo et al. (2020) studied the general energy transport pathways between the upper and lower layers and the eastern and western parts of the Gulf using a numerical model. They found that energy is transferred downward in the eastern part below the area delimited by the mean LC position, and in the western part (west of 94°W) possibly related to the LCEs interaction with the western bathymetry.

Despite all the research carried out, it is recognized that understanding of the relationship between the upper and lower layers of the GoM is still incomplete. This is in part due to the absence, in the past, of a more comprehensive depiction of the deep GoM circulation from observations, which in turn limited the assessment of the performance of numerical models in simulating the basic deep circulation patterns (Oey 2008; Morey et al. 2020). Most previous studies are region-limited, mainly focused on the eastern GoM basin, and time-limited, covering only a relatively short period. By being region-limited, the evolution of the obtained circulation patterns and their variability is incomplete and their connection with other GoM regions is missing. The short period considered in previous studies implies that only a few events were considered to obtain the GoM circulation patterns, which raises doubts about their recurrence and limits the description of their variability. Additionally, there is uncertainty as to whether some deep features are part of the mean fields or whether they are episodic and depend on the position and extent of the LC and LCEs, and deep eddy fields. To improve our understanding of the GoM circulation and establish their recurrent circulation patterns and their associated variability, long-term studies are needed.

This work aims to study the upper–lower coupled variability in the GoM. Three specific subjects are investigated:

1) The covariance of the upper and lower layers over the entire GoM.
2) The principal modes of coupled variability between the surface and near-bottom layers: their structure and the associated circulation patterns.
3) The dominant time scales of variation of the principal modes.

To achieve these goals, a long-term simulation of the GoM was carried out using the Hybrid Coordinate Ocean Model (HYCOM). Then, the Hilbert empirical orthogonal function (HEOF) technique was applied to the thickness of the upper and lower layers, in order to identify its coupled variability. Methods are described in section 2; the results and discussion are presented in section 3, including the resulting modes of variability with a description and analysis of the recurrent circulation patterns in each layer, and the time scales in which they vary. Also in this section, the propagation of coupled variability for different developmental stages of the LCS is examined. Conclusions are presented in section 4.

2. Methods

a. *The numerical simulation*

In this study, a free-running simulation of the circulation in the GoM was configured using the HYCOM model. HYCOM uses a generalized hybrid vertical coordinate system that allows vertical coordinates to follow isopycnal layers in the deep stratified ocean and transition to pressure coordinates in unstratified regions or to terrain-following coordinates in coastal areas (Chassignet et al. 2006). The horizontal domain covers the GoM, the northwestern Caribbean Sea, and part of the western North Atlantic Ocean (98°–77°W, 18°–32°N), with a spatial resolution of 1/25° (~3.8–4.2 km) and 27 hybrid vertical layers, which are mainly isopycnal layers in the open ocean below the mixed layer and z layers above it. The model bathymetry is an integration from different sources: the one from the HYCOM website (hycom.org), the General Bathymetric Chart of the Oceans (GEBCO), and corrected data from different sources, mainly observations collected during several cruises.

The experiment has biweekly open boundary conditions derived from a climatology produced by four years (2000–03) of a free-running simulation of the 1/12° Atlantic HYCOM. Following spinup, the model was run for 21 years with atmospheric forcing derived from hourly fields of a Weather Research and Forecasting (WRF) Model reanalysis of the period 1992–2011, without tidal forcing. The 21-yr record of surface forcing from WRF consists of eight nominal variables: vector wind stress, 2-m air temperature, sea surface temperature, 2-m atmospheric humidity, surface shortwave and longwave heat fluxes, surface atmospheric pressure, and precipitation. Climatological flow from 41 rivers along the coast of the GoM is also prescribed. The outputs of the model were recorded every day.

The simulation is not constrained by data assimilation; therefore, the positions of the LC and LCEs do not necessarily match observations at a specific time. This feature was required for this study so that the GoM circulation dynamics evolve naturally, satisfying the dynamics of a primitive equations model. By including all the processes involved in the GoM dynamics and offering a highly realistic representation of its hydrodynamics, the resulting coupled circulation patterns between the upper and lower layers are likely to be physically meaningful and accurately represent the GoM dynamics.

VALIDATION OF THE MODEL

The validation of the modeled circulation consisted in verifying that the major features in the upper and lower layers of the GoM were in statistical agreement with those reported in the literature based on observations. The validation is synthesized in Fig. 1. In general, the simulation is able to reproduce the intrinsic variability of the GoM and the more energetic patterns, including their amplitude, location, and evolution. The standard deviation of sea surface height (SSH) (Fig. 1a) depicts a primary area of high values within the LC extension and retraction region and a secondary area to the west of the GoM, in the otherwise known LCE graveyard. For the analysis of the LCE behavior and trajectories, an objective tracking technique was applied to the 21-yr record of near-surface velocity fields identifying a total of 30 LCE separation events, yielding a mean LCE separation period of 8.4 months, which is consistent with the altimetry record for 1993–2012 (Hall and Leben 2016). The structure of the mean along-channel velocity through the Yucatan Channel (Fig. 1d) and the Florida Straits (Fig. 1e) for the 21 years of the simulation is consistent with observations. The Yucatan main current, countercurrent, and undercurrent are overall well represented, with the core of the main current placed at ~86.3°W. The distribution of LCE separation periods (Fig. 1h) and propagation trajectories (Fig. 1b) are in good agreement with observations (Fig. 1c) (Sturges and Leben 2000; Vukovich 2007; Donohue et al. 2008), and other numerical studies (Dukhovskoy et al. 2015). The mean upper layer thickness (Fig. 1f), resembles the long-term mean SSH with the typical LC intermediate-stage configuration, with the LC reaching 89°W and 27°N. The mean lower layer circulation (Fig. 1g) reveals the dominant patterns reported by Pérez-Brunius et al. (2018) and Morey et al. (2020) (Fig. 1i), showing similar strength.

b. Estimation of the upper–lower coupled variability

To estimate the coupled variability between the upper and lower GoM, the HEOF technique was used. This technique characterizes the state of a system in terms of statistical modes of variability and its temporal rate of change (von Storch and Zwiers 1999). Under certain circumstances, this analysis can identify propagating features in the analyzed data for frequency band-limited signals (Horel 1984; Cromwell 2006). Therefore, nonstationary patterns, like the LC and LCEs, may require a greater number of modes to be adequately represented. In this work, the analyzed data comprise the variability of the thickness of two separate layers in the GoM. Therefore, the resulting coupled patterns are expected to represent meaningful relationships between the upper and lower Gulf variability. This choice is based on the representation of the GoM in terms of an upper (0–800 m) and a lower (below ~1000 m) layer, as proposed by Hamilton et al. (2018). Since the LC and LCEs are approximately in geostrophic balance, the isopycnal layer thickness contours, as well as the SSH contours, closely follow the streamlines in the flow. Thus, it is assumed that the layer thickness variability is a good representation of the mesoscale field variability.

The thickness data were obtained from the daily native outputs of the simulation: an upper layer representative of the surface, ranging from 0 m to approximately 250-m depth, obtained by summing the thickness of layers 1–19 of the model, corresponding to reference densities of $\sigma = 17.25$ and $\sigma = 26.52$ respectively; and a lower layer representative of the deep Gulf, ranging from approximately 1000- to 1800-m depth, obtained by considering the thickness of the 26th layer, corresponding to a reference density of $\sigma = 27.74$ of the model simulation. This choice of delimiting the surfaces allows us to obtain large amplitudes of the layer-thickness signature and prevents the layers from coming into direct contact, so the upper and lower fluctuations would not be a mirror of each other, reflecting the covariability between them. For each grid point, the trend and annual cycle were removed from the time series, and variations on time scales shorter than 30 days were removed using a Lanczos low-pass filter in order to focus on mesoscale features. The data from the upper and lower layers were combined into an array to which the Hilbert transform was applied, and the corresponding complexified matrix was composed. Then, the covariance matrix was computed, and the Hilbert EOFs were obtained. A brief description of the HEOF technique is presented in the appendix.

3. Results and discussion

a. Coupled circulation patterns in the surface and near-bottom layers

The HEOF technique revealed that the first four modes of coupled variability are not degenerate, according to the rule of North et al. (1982), and contain approximately 50% of the total variance, with fractions of 23%, 12%, 8%, and 6% respectively. HEOFs [$\boldsymbol{\phi}$ in Eq. (A2)] for each layer were obtained and displayed using polar coordinates, with the spatial amplitude [$\mathbf{A}$ in Eq. (A5)] shown in color shading and the spatial phase [$\boldsymbol{\theta}$ in Eq. (A5)] presented as vectors (Fig. 2). Since the real and imaginary components of the HEOFs are shifted one-quarter wavelength, variations in the spatial phase can be used to infer signal propagation in accordance with the sign convention used by Cromwell (2006), in which progression in time corresponds to an anticlockwise rotation of the eigenvector phase. Phases have an arbitrary origin, and therefore the direction of a phase vector at any particular geographic location is not important. What matters is whether and in what

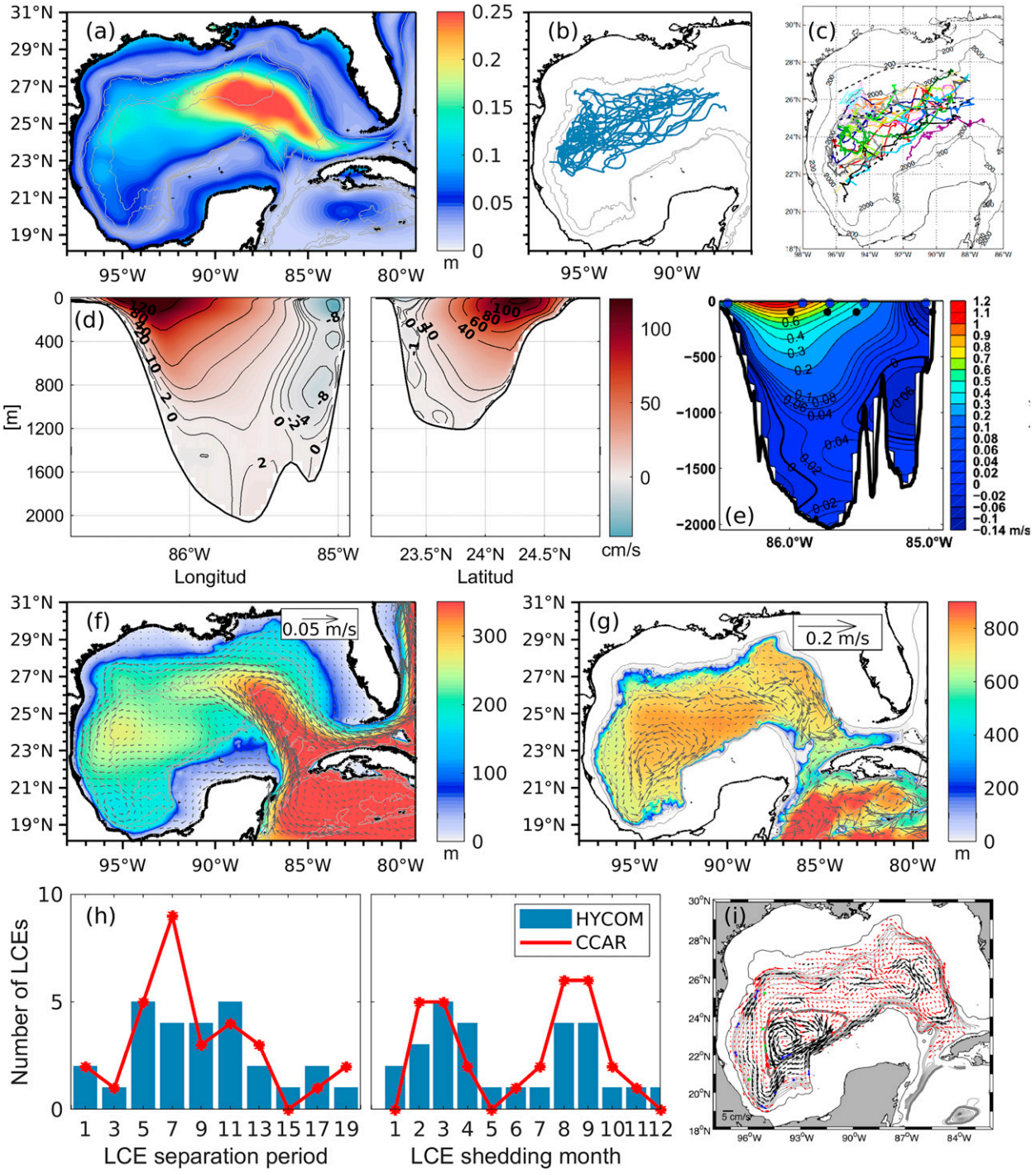

FIG. 1. HYCOM validation: (a) standard deviation of the SSH from HYCOM and observations, (b) trajectories of every LCE from HYCOM simulation, (c) trajectories of every LCE from observations [from Donohue et al. (2008)], (d) mean along-channel velocity component in the Yucatan Channel and Florida Straits from HYCOM, (e) mean along-channel velocity component in the Yucatan Channel from observations [from Athié et al. (2015)], (f) time-averaged upper-layer thickness (color contours) and velocity (vectors) from HYCOM, (g) time-averaged lower-layer thickness and velocity from HYCOM, (h) comparison of frequency distributions of LCE shedding period and monthly occurrence between HYCOM and CCAR database, and (i) mean deep velocity from observations [from Pérez-Brunius et al. (2018)].

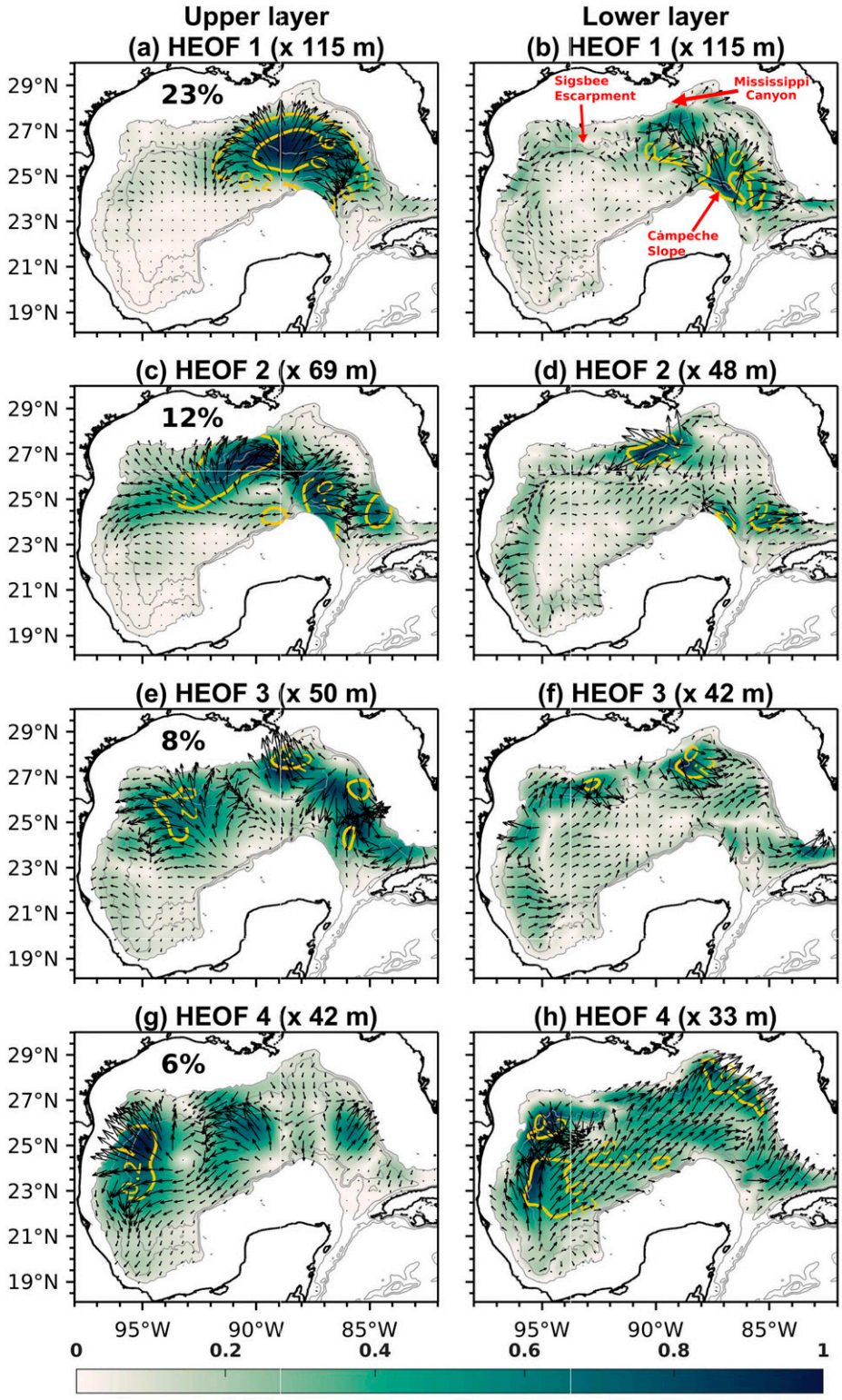

FIG. 2. Leading HEOF modes of coupled variability in the Gulf of Mexico for the (left) upper layer and (right) lower layer. The spatial amplitude is shown in color shading, normalized by the maximum value (in parentheses); the spatial phase is presented as vectors; yellow contours represent the proportion of explained variance, and gray contours represent the 500-, 1000-, 2000-, and 3000-m isobaths. The percentage of the total variance in each mode is also indicated.

sense the direction of the phase vector changes from one location to another.

In the upper layer, the first mode (23%) (Fig. 2a) displays an area with large amplitude values, representing anomalies between ±100 m approximately, that covers the region where the extension and retraction of the LC occurs. The organized and smooth anticlockwise rotation of the spatial phase over the high amplitude region indicates strong propagation of the thickness anomalies from southeast to northwest, coincident with the propagation of the LC tip over the same region. In the lower layer (Fig. 2b), the regions with the highest amplitude have a corresponding anomaly in the upper layer, although with a slight location shift and a different pattern, following certain bathymetric features. Propagation to the west is deduced from the phase rotation of the anomalies in the eastern basin and those along the 3000-m isobath.

On the other hand, the second, third, and fourth modes represent 26% of the total variance together. In the upper layer, the second and third HEOFs show regions of high amplitude over the central and eastern Gulf accentuated in the Sigsbee Escarpment, the eastern plain centered at 23.5°N, 85°W to the northeast of the Campeche slope, and the West Florida Shelf (Figs. 2c,e). According to the spatial phase, variability in the first two regions propagates to the west, whereas the third feature propagates toward the east and southeast. The lower layer displays regions of large amplitude in correspondence with those of the upper layer, with most of its variability located along steep bathymetric features in the Sigsbee Escarpment, the Campeche slope, and along the northern boundary of the GoM (Figs. 2d,f). The fourth mode of the upper layer (Fig. 2g) displays an area with high amplitude over the northwestern GoM, west of 93.5°W and north of 22°N, with propagation of the thickness anomalies from northeast to southwest. Concerning the lower layer, there are anomalies corresponding with those in the upper layer aligned with the 3000-m isobath in the western boundary and over the Sigsbee plain (Fig. 2h). The lower layer anomalies at the western boundary propagate from north to south, whereas the anomalies over the Sigsbee plain have no clear propagation pattern and seem to oscillate uniformly.

To find coupling relationships between the upper and lower layers and the associated circulation patterns, the evolution of the layer thickness anomaly field for the entire simulation period was reconstructed using Eq. (A9), employing the four leading HEOFs together and then each one separately. Such reconstructions are represented as figures which include the original layer thickness anomalies in order to compare how well the reconstruction is performed (Figs. 3a,c,e,g,i,k,m,o and 4a,c,e,g,i,k,m,o), and incorporate the model velocity vertically averaged over each isopycnal layer, and the 17-cm SSH contour. Additionally, the reconstructions are included in the online supplemental material as movies. In general, the results show a first-order correspondence between the layer thickness anomalies and circulation, with a positive anomaly related to an anticyclonic circulation and a negative anomaly to a cyclonic circulation. While the above is always true for the upper layer, such correspondence is not always observed in the lower layer.

The reconstruction using the first HEOF (movie 1 in the supplemental material) shows a relationship between the layer thickness anomalies: a thickening of the upper layer corresponds to a thinner lower layer and vice versa. It is observed that during events of LC intrusion, the upper-layer positive anomaly, associated with the anticyclonic circulation of the LC (Fig. 3b), is accompanied by a lower-layer negative anomaly, which is the expression of a deep anticyclone (Furey et al. 2018; Yang et al. 2020) (Fig. 3d). As this deep negative anomaly further penetrates to the northwest, in phase with the LC intrusion (Fig. 3f), a positive anomaly with cyclonic circulation forms behind it, establishing the well-known anticyclonic–cyclonic eddy pair (Welsh and Inoue 2000; Lee and Mellor 2003; Yang et al. 2020) (Fig. 3h). Then, to the eastern edge of a fully extended LC (Fig. 3j), an upper-layer negative anomaly amplifies in concert with the lower-layer positive anomaly (Fig. 3l) and propagates together anticyclonically along the LC, but with a slight vertical location shift with the lower anomaly leading the upper anomaly. These anomalies, which manifest as a cyclone extending the full water column, cleave the LC and eventually develop a necking causing a LCE to detach, following a mechanism similar to that described by Donohue et al. (2016b) (Figs. 3n,p). Nevertheless, several LCE reattachment events can occur before its final separation, in which case the process is partially repeated. During the entire simulation, a total of 28 events were observed where this coupling process led to final separation of LCEs.

The reconstruction of the layer-thickness anomalies using the four leading modes together (movie 5 in the supplemental material) can help us identify additional circulation patterns associated with the high-amplitude regions described above. The movie reveals that, in the upper layer: 1) the separation and western translation of LCEs, 2) the southward propagating meanders on the eastern side of the LC, 3) the retraction of the LC, and 4) the reattachment of large LCEs are well described by the layer-thickness anomalies, in agreement with Oey (2008), Chang and Oey (2013), Zeng et al. (2015), Liu et al. (2016), Yang et al. (2020). The duration, intensity, and frequency of such events are variable and depend on the stage of penetration of the LC and the LCE size.

In the lower layer, only the larger-scale features are generally well resolved over the deep Gulf, with the exception of distinctive smaller-in-size characteristics in the eastern basin related to the LC variability. Nevertheless, among the upper-layer processes described above, the separation and western translation of LCEs and the southward propagation of meanders alongside the LC have a clear lower layer response. The separation process was described at the beginning of the section, and we proved that is well explained by HEOF 1. The meanders in the upper layer precede LCE shedding events most of the time and manifest as an alternation of positive and negative anomalies inside and outside the eastern branch of the LC, representing an anticyclone and a cyclone, respectively (Zavala-Hidalgo et al. 2003; Donohue et al. 2016a). The lower layer response manifests as a shrinkage of the layer under a positive anomaly of the upper layer and as a stretching under a negative anomaly, which is more intense to the south of the West Florida Shelf. Movie 5 (in the supplemental

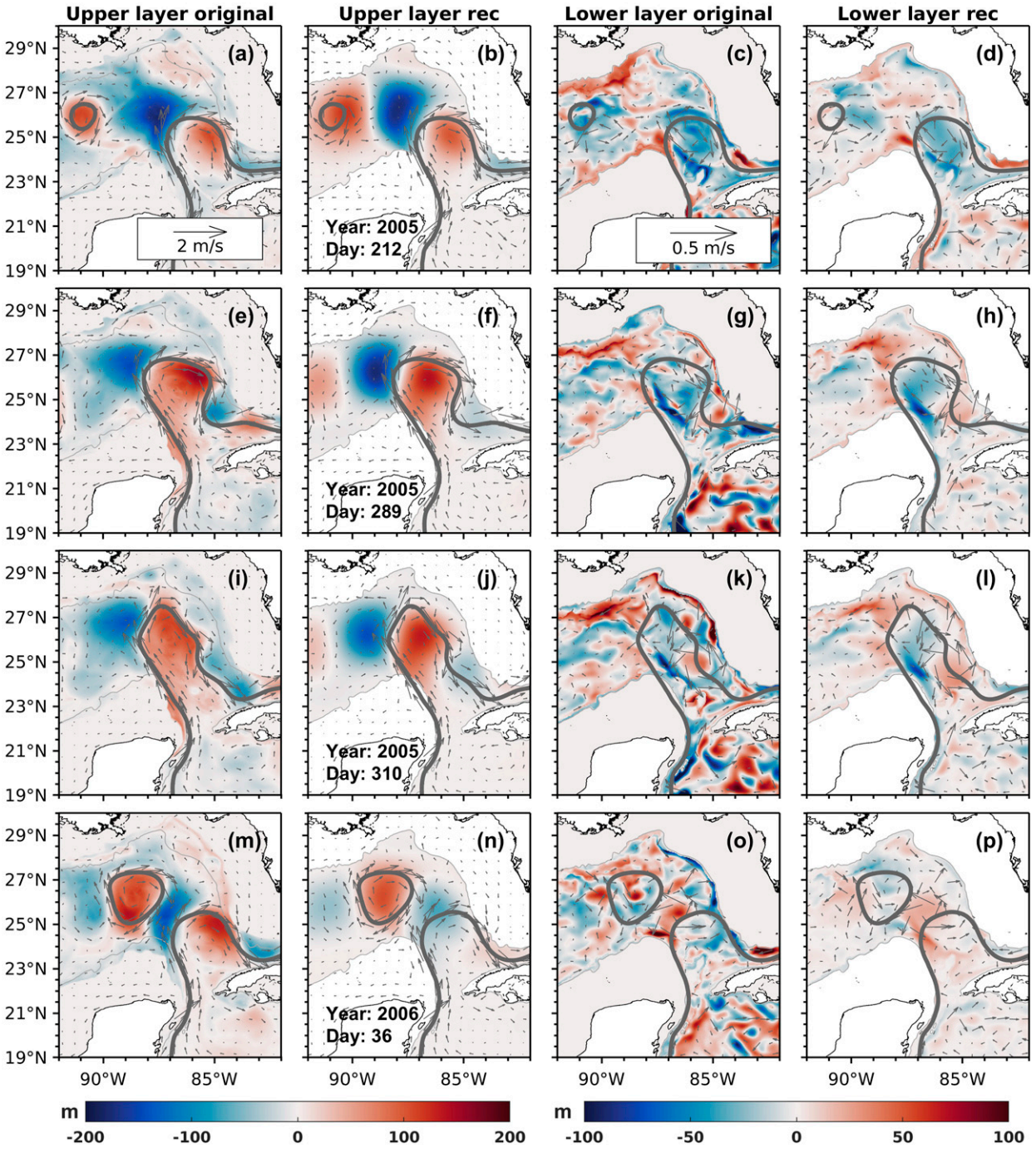

FIG. 3. Snapshots of (a),(e),(i),(m) original and (b),(f),(j),(n) reconstructed upper-layer thickness anomalies, and (c),(g),(k),(o) original and (d),(h),(l),(p) reconstructed lower-layer thickness anomalies for a LCE separation event from model year 2005, day 212 to model year 2006, day 36. For the reconstructed fields, only HEOF 1 was used. The corresponding snapshots of model velocity (vectors) vertically averaged over each layer and the 17-cm SSH contour (thick gray contour) are also shown.

material) shows that the relationship between these layer-thickness anomalies is related to the coupling of upper and deep eddies, mainly described for HEOF 1 above. Underlying this behavior, different processes are involved in the formation and detachment of LCEs, such as the development of baroclinic instability under the LC and the increase of EKE (Donohue et al. 2016b).

An example of the coupling between the upper and lower layers during the western propagation of a LCE, using the reconstructed layer-thickness anomalies for the first four modes,

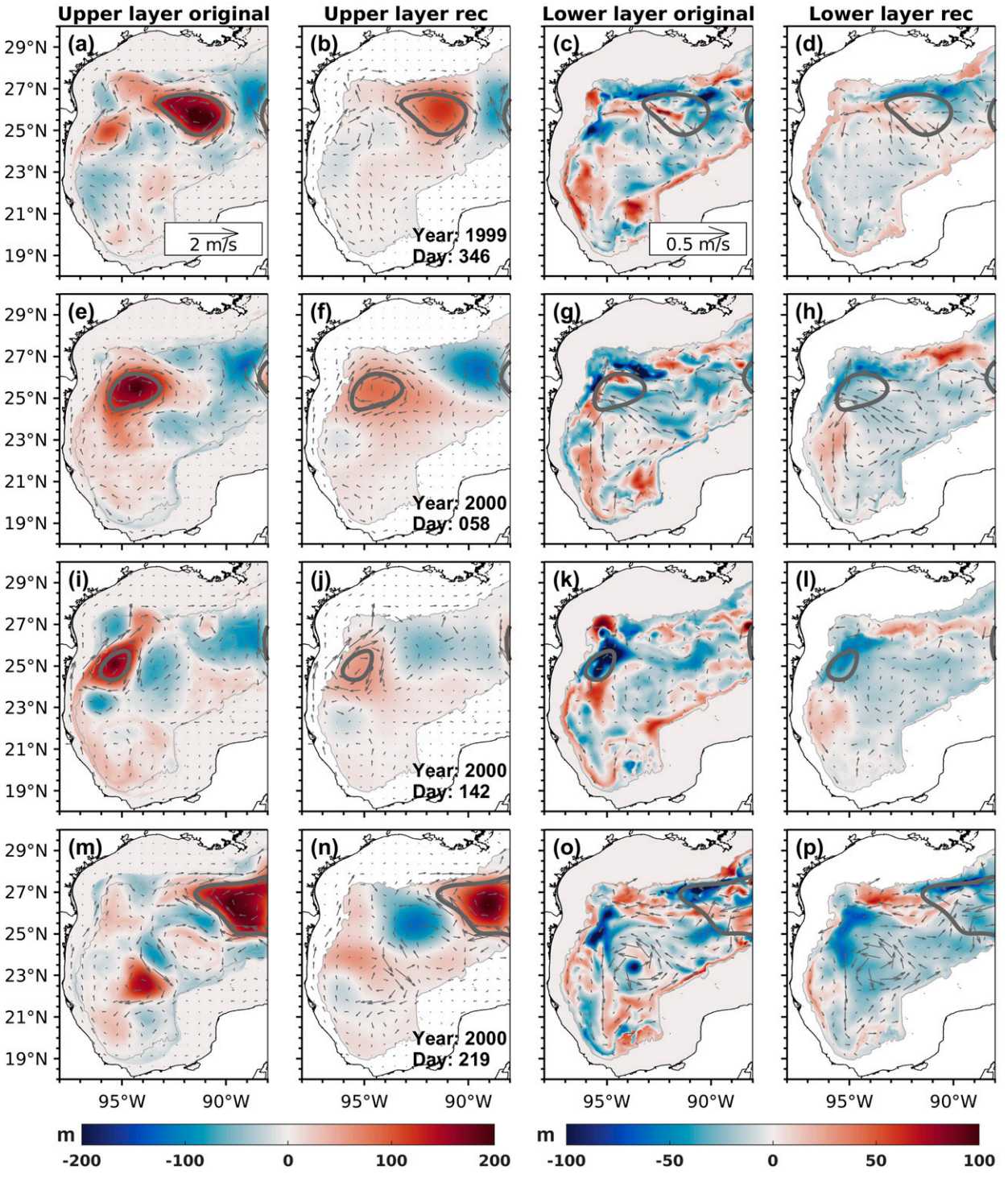

FIG. 4. Snapshots of (a),(e),(i),(m) original and (b),(f),(j),(n) reconstructed upper layer thickness anomalies, and (c),(g),(k),(o) original and (d),(h),(l),(p) reconstructed lower layer thickness anomalies for a LCE westward propagation event from model year 1999, day 346 to model year 2000, day 219. For the reconstructed fields, HEOFs 1–4 were used. The corresponding snapshots of model velocity (vectors) vertically averaged over each layer and the 17-cm SSH contour (thick gray contour) are also shown.

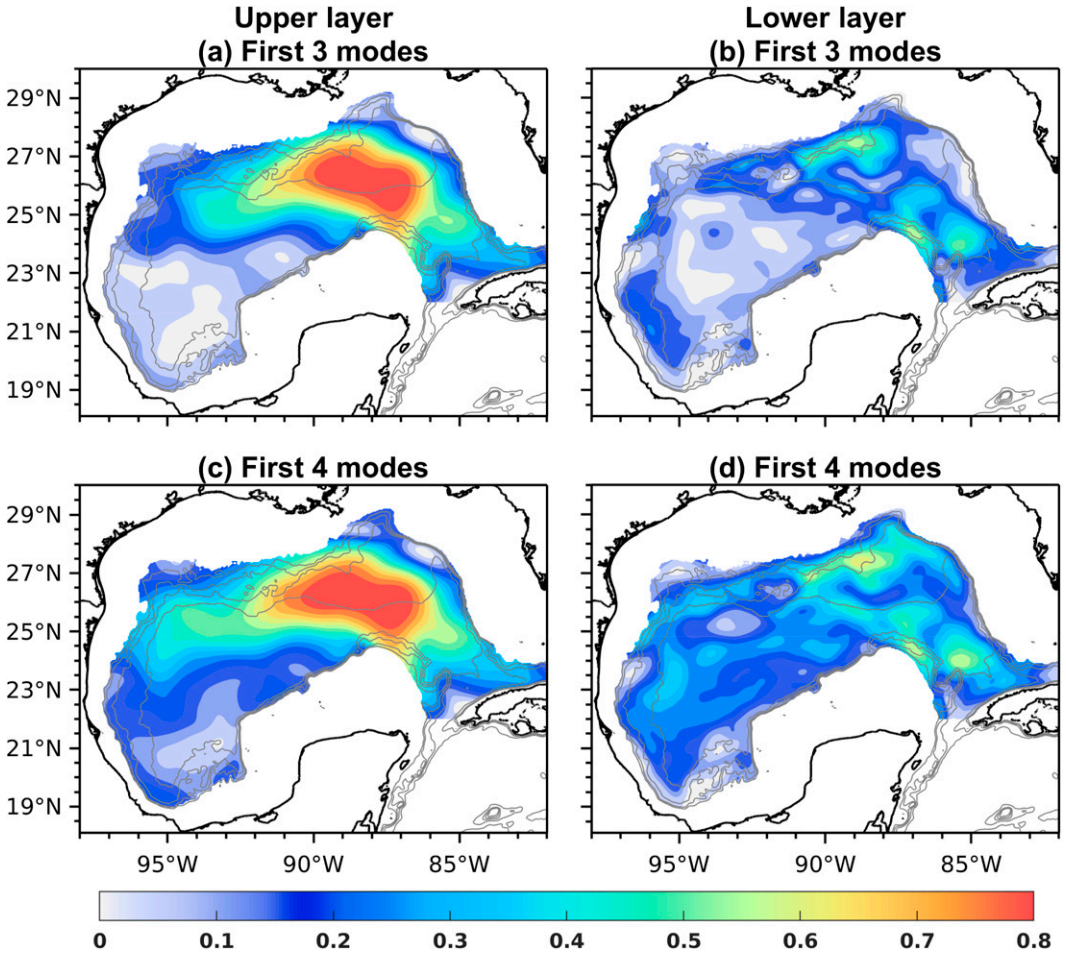

FIG. 5. Maps of the proportion of explained variance for the reconstructed upper- and lower-layer thickness anomalies using (a),(b) the three leading HEOFs and (c),(d) the four leading HEOFs. The gray contours represent the contours f/H ([1:5] $\times 10^{-8}$ m^{-1} s^{-1}), where f is the local Coriolis parameter and H is the bottom depth.

is shown in Fig. 4. In Fig. 4b, a large anticyclone centered around 26°N, 91°W is associated with a positive anomaly in the upper layer. In the lower layer (Fig. 4d), a negative anomaly between the 1000- and 2000-m isobaths, related with divergence of the flow, is located north of the LCE. It is important to note that a well-defined anticyclone–cyclone dipole is observed in the velocity field under the LCE, although with no anomaly pattern associated, and that the Sigsbee Gyre is very weak, almost nonexistent. Approximately 2.5 months later, when the LCE has reached the northwestern boundary of the GoM (Fig. 4f), in the lower layer the negative anomaly has traveled to the northwest, and the deep cyclone, originally to the rear of the LCE, has propagated anticyclonically to the south of the eddy (Fig. 4h), intensifying the Sigsbee Gyre as it incorporates in it. At this point, a positive anomaly in the western arm of the gyre seems to be related to such intensification (Fig. 4h). After a period of being stationary for ~3 months, the LCE has traveled slightly south with the lower-layer negative anomaly nearly corresponding vertically, and the deep cyclonic gyre weakened (Figs. 4j,l). Within the next 2 months, the LCE undergoes a fast translation to the south reaching ~23°N (Fig. 4n), simultaneously a new cyclone in the lower layer seems to form behind the LCE following it, but with a more marked negative anomaly, which is partially resolved in the reconstructed data (Fig. 4p). Eventually, this new deep cyclone reintensifies the Sigsbee Gyre.

These reconstructions indicate that the main processes represented by the four leading HEOFs are consistent throughout the entire simulation period; thus, the circulation patterns found can be regarded as recurrent patterns. The reconstructions also suggest that a complete representation of nonstationary propagating features, like the LC and LCEs, is not feasible using techniques like EOFs, HEOFs, or self-organized maps (von Storch and Zwiers 1999; Cromwell 2006; Meza-Padilla et al. 2019). However, the use of HEOFs and their spatial and temporal phases provide insights and a first-order description of the propagation of these features in the GoM.

Maps of the proportion of explained variance [Eq. (A12)] of the reconstructed upper- and lower-layer thickness anomalies using the three leading HEOFs complement the results that the upper variability associated with these HEOFs is mainly located in the eastern GoM basin, east of 92°W (Fig. 5a), and that the

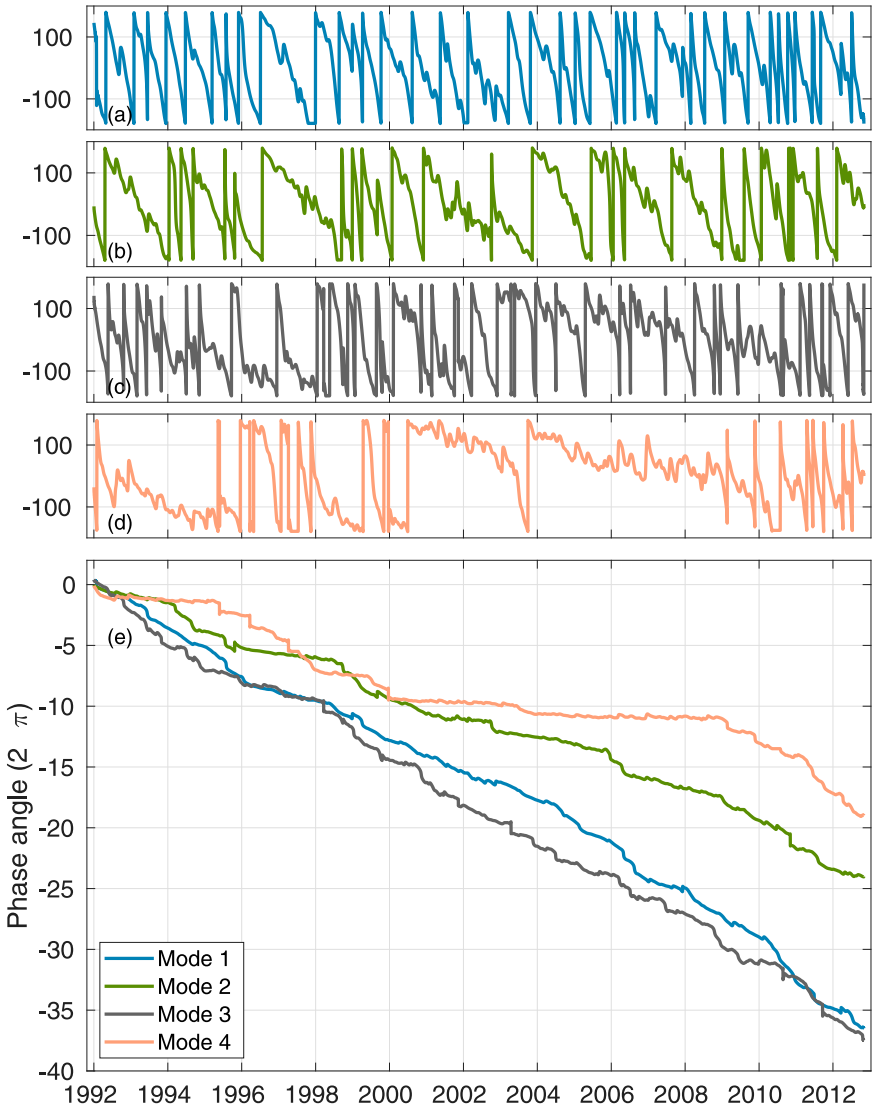

FIG. 6. (a)–(d) Time series of the temporal phase for the four leading modes (°), and (e) the unwrapped phase for the same modes (in units of number of cycles or multiples of 2π).

lower-layer variability is located over the slope (Fig. 5b). The lower layer map (Fig. 5b) shows that the larger anomalies are aligned with the planetary potential vorticity (f/H) contours, where f is the local Coriolis parameter and H is the bottom depth.

b. *Dominant time scales of the coupled variability*

To investigate the dominant time scales of the coupled variability, the temporal phase of the principal components (PCs) [the ψ term in Eq. (A6)] is analyzed. For a given mode, the time variation of the temporal phase $\psi(t)$ provides information about quasi-periodicities in the data. If $\psi(t)$ decreases monotonically from 180° to −180° over any 360° interval, it can be inferred that a certain cyclicity exists in the coupling. The temporal phases for the four leading HEOFs and their corresponding unwrapped phase are shown in Fig. 6. The unwrapped phase was computed by subtracting a factor of 2π every time a phase cycle was completed, with its slope providing information about the phase speed.

The first mode shows a clear periodicity, namely a quasi-steady decrease from 180° to −180° with an average period of 7 months (Fig. 6a), close to the observed mean LCE separation period of 8.4 months in the model simulation and the altimetry record reported by Leben (2005) and Hall and Leben (2016). Its behavior is consistent with the episodic nature of a LC extension and retraction cycle. Its unwrapped phase (Fig. 6e) displays a quasi-linear evolution with time, consistent with the definition of cyclicity. The temporal phase for the second mode (Fig. 6b) shows a more irregular periodicity, with longer time scales of approximately 10.5 months on average and still a quasi-cyclic behavior but with some leaps. Such features are mainly related to short retractions of the LC and reattachments

TABLE 1. Dominant time scales for the four leading modes according to the temporal phase of the PCs.

Mode	Percentage of the total variance	Mean period (months)	Mean cycles per year
1	23	7	1.7
2	12	10.5	1.1
3	8	6.7	1.8
4	6	14	0.9

or changes in the LCE shape. However, they are almost always coincident with minimal amplitude values and therefore do not contribute much to the overall variability of the mode. Its unwrapped phase displays periods of variable phase speed. Concerning the temporal phase of the third mode (Fig. 6c), its cyclicity is less noticeable but still perceptible, with an average period of 6.7 months associated with high-frequency variability, specifically from 1998 to the end of the record, which is also deduced from the marked acceleration of its unwrapped phase after this year (Fig. 6e). The relatively short mean period of this PC mode is related to strong meandering and LCE shedding events followed by a reattachment.

For the fourth mode, the cyclicity is even less noticeable (Fig. 6d). Rather, there seems to be a preference for the phase to spend more time in a given value or stage for specific periods lasting 14 months on average. The above suggests the persistence of a pattern, which may be strongly related to the presence of LCEs and mesoscale circulation in the western basin. The behavior of the unwrapped phase for this mode is more staggered than for the previous ones (Fig. 6e). Table 1 shows a summary of the characteristics of the temporal phases.

c. *Propagation of the coupled recurrent circulation patterns*

To assure statistical consistency of the results through time, discussion of the propagation of coupled patterns between the upper and lower layers is done with a composite analysis considering the entire simulation period (1992–2012). The HEOFs technique provides a measure of the spatial and temporal connection between the layers, allowing to identify, to a first order, coupling of circulation features that are not collocated in time nor space between the layers. Two analyses were carried out. The first analysis describes the LC intrusion and LCE separation events considering the first HEOF in the eastern GoM. The second analysis describes the joint contribution of the four leading HEOFs for different LCS developmental stages in the entire GoM basin.

For the first analysis, composites of reconstructed layer thickness anomalies at different times t centered around different temporal phase values $\psi(t)$, were computed for the first HEOF. Using six frames separated by 1/6th of a period (60° or $\pi/3$), the chosen temporal phase values in degrees were $\psi = 180°, 120°, 60°, 0°, -60°$, and $-120°$. The choice of the first value is arbitrary, which for simplicity was chosen to be 180°. Then, the means of the reconstructed fields were computed over the times corresponding to each of these phase angles. The six frames of these composites are displayed in Fig. 7, along with the corresponding composites of model velocity vertically averaged over each layer and the 17-cm SSH contour, representing a life cycle whose duration is 7 months on average (Table 1). Note that layer-thickness anomalies for phases shifted 180° (π) are identical but with opposite signs (Table A1).

The results reveal that the different frames correspond to different stages of the LC intrusion–retraction and LCE separation processes. The frame for the 180° composite roughly corresponds to the state of the system when a LCE is just detached from the LC, while the following phases correspond to the western propagation of the LCE and a new LC intrusion cycle. An inspection of such maps allows detection of signal propagation in a statistically consistent manner, and therefore, corroboration of the recurrence nature of the coupling between the upper and lower layers during the LCE separation process described in section 3a for a single event of the model data.

In the upper layer, each of the different phases is characterized by a train of four anomalies of alternate signs, with two regions of positive anomalies and two of negative anomalies. The 180° composite displays a positive layer thickness anomaly centered around 26°N, 90°W, which is associated with a strong anticyclonic circulation and a closed 17-cm SSH contour, an LCE. A negative anomaly is located to the west of the LCE and another between the LCE and the LC. As will become evident from the remaining phase composites, the latter corresponds to the remnants of the cyclone responsible for tightening the LC. As time progresses, the anomalies propagate to the northwest in a circuit fashion between 93° and 83°W. The predominant positive anomaly at 26°N, 90°W weakens as it spreads westward and is accompanied by the intensification and northwestward propagation of the eastern negative anomaly (180°, 120°, and 60° composites). At the time of the 120° composite, a positive anomaly located around 25°N, 86°W amplifies as it propagates northwestward following the LC front during the 60°, 0°, −60°, and −120° composites. During these phases, a negative anomaly related to a cyclonic circulation develops along the eastern branch of the LC, tightening the LC. Finally, in the −120° composite, the configuration of the anomalies is representative of a LC in an extended stage with a cyclonic circulation in its neck. Eventually, the cyclone produces a necking of the LC, which favors the intensification of a closed anticyclonic circulation on the tip of the LC and the eventual separation of a LCE, which coincides with the negative anomaly traveling farther west (180° composite).

In the lower layer, the train of four anomalies maintains opposite signs relative to those on the surface. However, the structure is more complex and less organized, with some of the features strongly determined by the bathymetry, as described in section 3a. After a LCE detachment, in the 180° composite, a deep negative layer-thickness anomaly characterized by an anticyclonic circulation begins to form below the upper-layer positive anomaly associated with the LC. As the LC intrudes the northern GoM, the negative anomaly propagates northwestward keeping its intensity but with a different extension through the 120° and 60° composites. After an intermediate stage of the LC is reached in the 60° composite, two positive

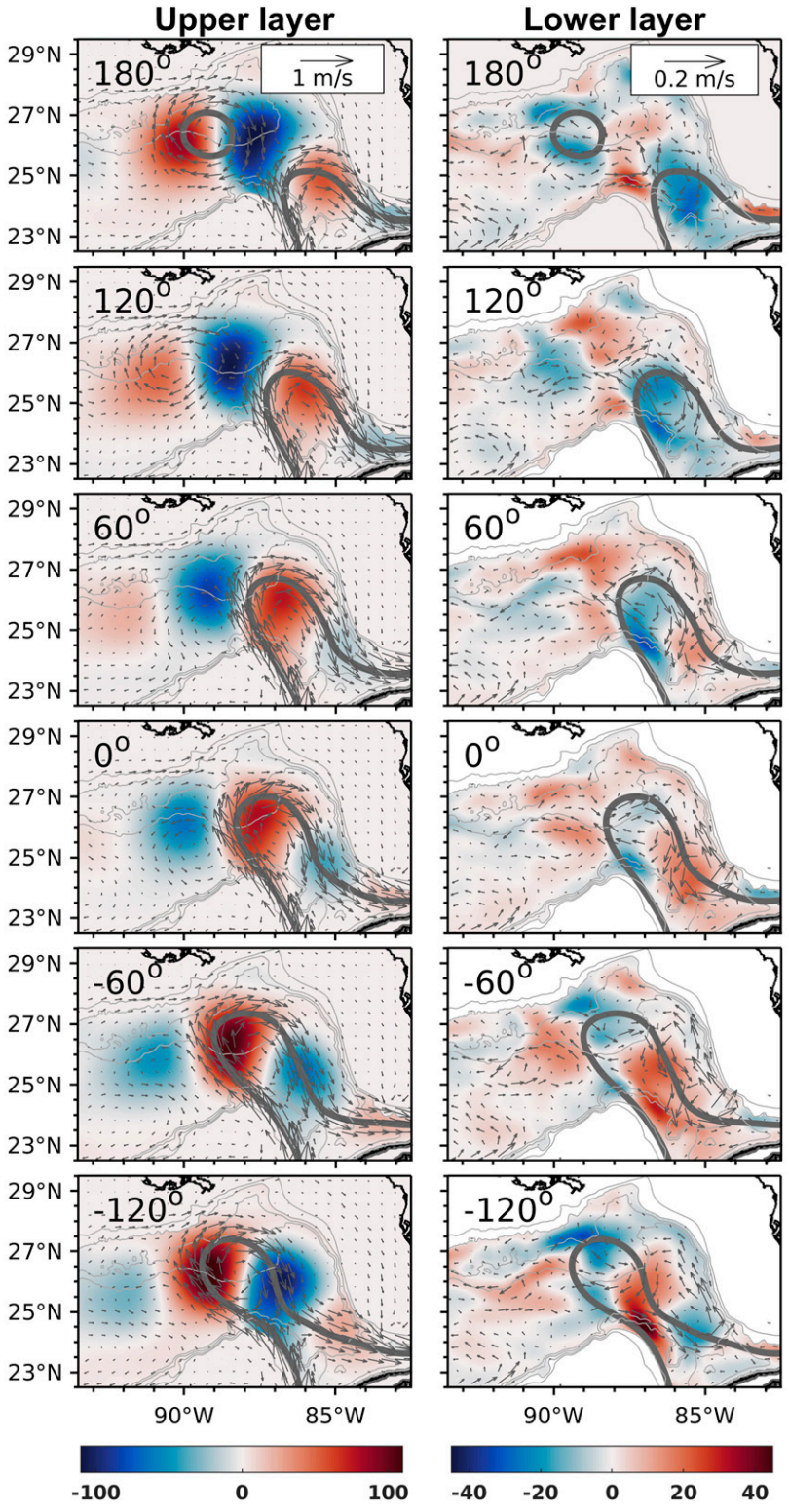

FIG. 7. Composites of reconstructed (left) upper- and (right) lower-layer thickness anomalies for 180°, 120°, 60°, 0°, −60°, and −120° phases of mode 1. The corresponding composites of model velocity (vectors) vertically averaged over each layer and 17-cm SSH contour (thick gray contour) in each phase stage are also shown.

anomalies associated with two cyclones in a north–south orientation are formed to the east of the negative anomaly. During the 60°, 0°, and −60° composites, the anomalies associated with a cyclone and a cyclone–anticyclone dipole are noticeable. The southern positive anomaly, wider than the northern one, represents the average deep expression of the cyclone covering the entire water column as a result of the baroclinic instability process described by Donohue et al. (2016b). From the 0° to −120° composite, this cyclone intensifies and propagates anticyclonically in concert with its upper counterpart, but showing the slight vertical shift also present in the example of section 3a, as the LC further penetrates and its tightening is more noticeable, while the northern cyclone keeps a constant intensity and undergoes a little drift to the west. Accompanying the evolution of these anomalies, regions of convergence and divergence of water masses are present during the LC extension cycle, mainly located along prominent topographic features, like the Campeche Slope, the DeSoto Canyon, and offshore the Mississippi Fan from the Mississippi Canyon to the Sigsbee Escarpment. The cycle concludes with the detachment of a LCE in the 180° composite and then the cycle repeats. The above indicates that the coupled process observed by Donohue et al. (2016b) is recurrent and dominant, with a time scale of variability consistent with the mean LCE separation period. Consequently, the deep eddies appearing in the mean field under the LC (Furey et al. 2018; Morey et al. 2020), are episodic and their structure depends on the position and extent of the LC.

The second analysis aims to examine the joint contribution of the four leading HEOFs to the overall variability in the upper and lower layers for different LCS developmental stages. To this end, composites of reconstructed layer thickness anomalies, summing up the first four modes, were computed for the main LC patterns and two incremental LCE positions during their westward drift. These composites were computed by seeking, over the entire 21-yr simulation, times when the LC and LCEs were located at the corresponding stages, and then averaging the reconstructed fields over such times. As a result, the number of events considered for each composite is not the same and is indicated in parentheses in the corresponding figure. Zeng et al. (2015) and Liu et al. (2016) conducted studies to characterize the main LC spatial patterns with the self-organizing maps (SOM) method using SSH data from altimetry products. The nature of the LC patterns they found is similar, with patterns accounting for strong LC intrusion, retracted LC, and different stages of the LCE shedding process. Thus, the LC patterns considered in this study emulate the three ones found by Zeng et al. (2015):

1) The LC intermediate pattern, with mean northward and westward intrusion of the LC contour of 26°N and 87.5°W, respectively.
2) The LC extended pattern, with the mean northward and westward intrusion of the LC contour of 27.5°N and 89°W, respectively.
3) The LC retracted pattern, in which a LCE has been detached, with the mean northward and westward intrusion of the LC contour of 24.5°N and 86°W, respectively, and the LCE approximately centered at (26°N, 88°W).

The two incremental positions of the LCEs during their westward translation were taken when the eddy is centered around 91°W (hereinafter referred to as the mid-eddy stage) and 95°W (hereinafter referred to as the western eddy stage). The composites of the reconstructed layer thickness anomalies for these five development stages of the LCS, are shown in Figs. 8 and 9.

On the eastern GoM basin (east of 92°W), the LC pattern for the retracted, intermediate, and extended stages (Figs. 8a–d and 9i,j) have a high correspondence with the 180°, 60°, and −120° phase composites only considering the first HEOF (Fig. 7). The correspondence is high in both the layer thickness anomalies and the model velocities; thus, the first HEOF describes well the dominant coupled circulation patterns along LC stages. The correspondence is stronger for the upper layer than for the lower layer. Hence, to a high degree, the upper-layer variability description is dominated by the first mode (refer to Figs. 5 and 7), whereas for the description of the lower-layer variability, the second, third, and fourth modes have a role that is small but not null. A difference between the lower-layer variability described by only the first mode and that described by the first four modes is the convergence and divergence of water masses in the northeast GoM, along the 2000 m-isobath from the DeSoto Canyon to the Sigsbee Escarpment.

In the northern GoM basin (north of 25°N) the primary source of layer thickness variability in the upper layer are the LC and LCEs. The central GoM basin (south of 25°N) has moderate variability, whereas there is minimal variability in the southern GoM (Bay of Campeche). In the western basin, north of 21°N, an anticyclonic circulation is maintained, disrupted by the passage of LCEs and their arrival to the western boundary. In the Bay of Campeche, there is a continuous presence of a cyclonic circulation, the Campeche Gyre centered around 20°N, 95.5°W, which changes its position and intensity during the cycle (Figs. 8a,c,e and 9g,i).

In the western lower layer, similar to what occurs in the eastern basin, the thickness anomalies are opposite to those in the surface. However, the lower anomalies are less intense and more dispersed than their corresponding ones on the surface (Figs. 8b,d,f, and 9h,j). For the LC stages with no presence of LCEs west of 90°W (i.e., for the retracted, intermediate, and extended stages; Figs. 8b,d,j), the lower anomalies are small and quite homogeneous, without clear evidence about the origin of their sign.

When a LCE has passed the 90°W longitude, important anomalies in the lower layer form along the boundary between the 1000- and 3000-m isobaths (Figs. 8f and 9h). In the mid eddy stage (Fig. 8f), the most pronounced anomalies are located below the LCE. Ahead of the LCE, there is a positive anomaly associated with a convergence of water, which drives a cyclonic circulation along the deep boundary. Behind the LCE, there is a negative anomaly associated with a divergence of water; and on the easternmost side there is a positive anomaly. The westward propagation these signals exhibit, probably involve TRWs (Hamilton 2009; Hamilton et al. 2019); however, a thorough description of the nature of these signals is beyond the scope of this work.

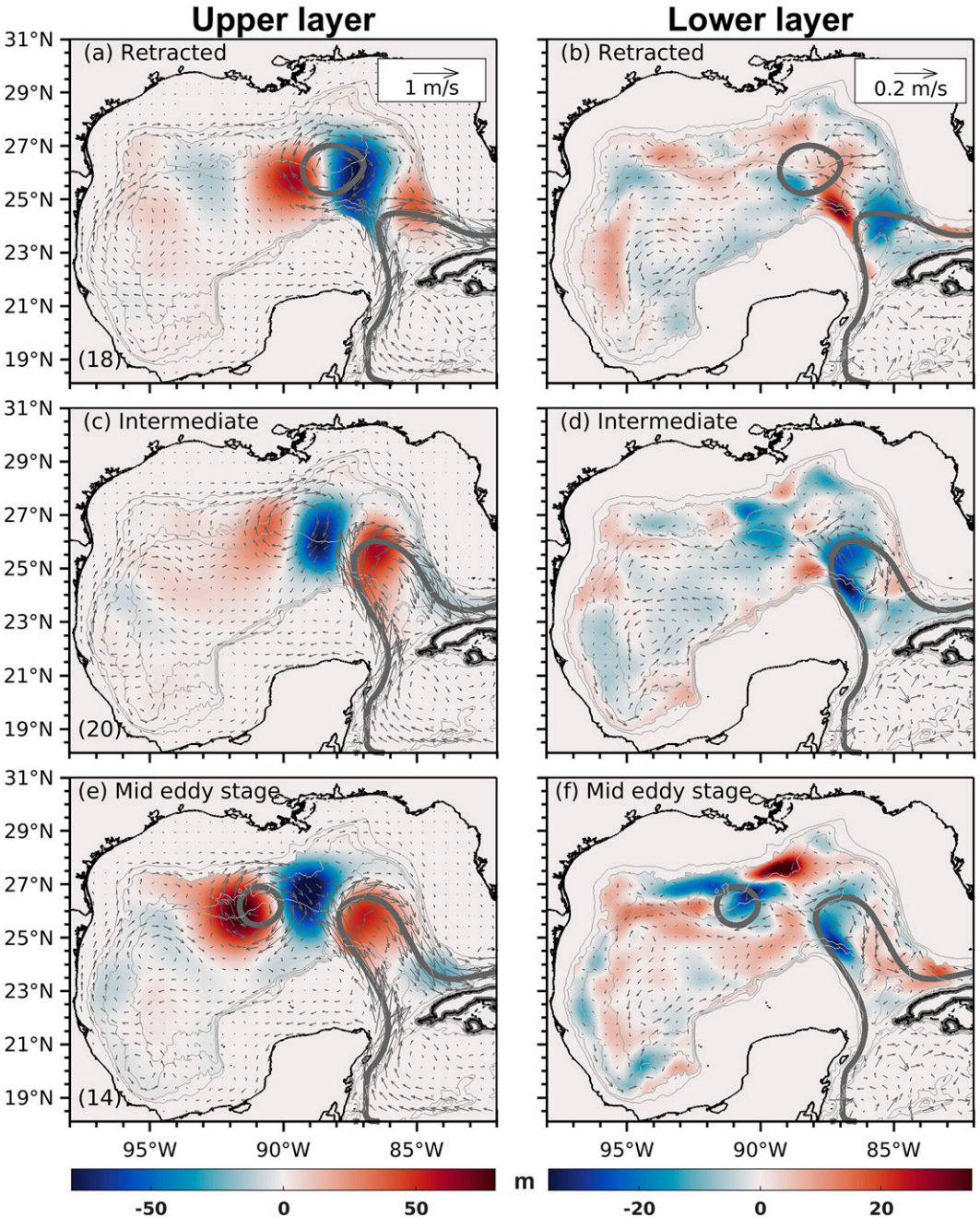

FIG. 8. Composites of reconstructed (left) upper- and (right) lower-layer thickness anomalies for different LC and LCE stages, considering the four leading modes: retracted, intermediate, and mid-eddy stage (LCE at ~91°W). The corresponding composites of model velocity (vectors) and 17-cm SSH contour (thick gray contour) in each stage are also shown. The number of events used to make the composites is indicated in the lower left corner for each stage.

In the composite corresponding to the western eddy stage (Fig. 9h), the structures in the lower layer have reached the northwestern basin but with wider and less intense anomalies than in the mid eddy stage (Fig. 8f). The leading positive anomaly is now south of the LCE, the negative anomaly is north of it, and the last positive anomaly is centered around 89.5°W along the 2000-m isobath (Fig. 9h). This configuration of the anomalies, which is consistent with the pattern found for a single event (section 3a; Fig. 4), is associated with the dissipation of the deep anticyclone of the modon and the southward translation of the corresponding deep cyclone, which strengthens the cyclonic circulation in the abyssal plain as documented numerically by Welsh and Inoue (2000), and observationally by Tenreiro et al. (2018) and Furey et al.

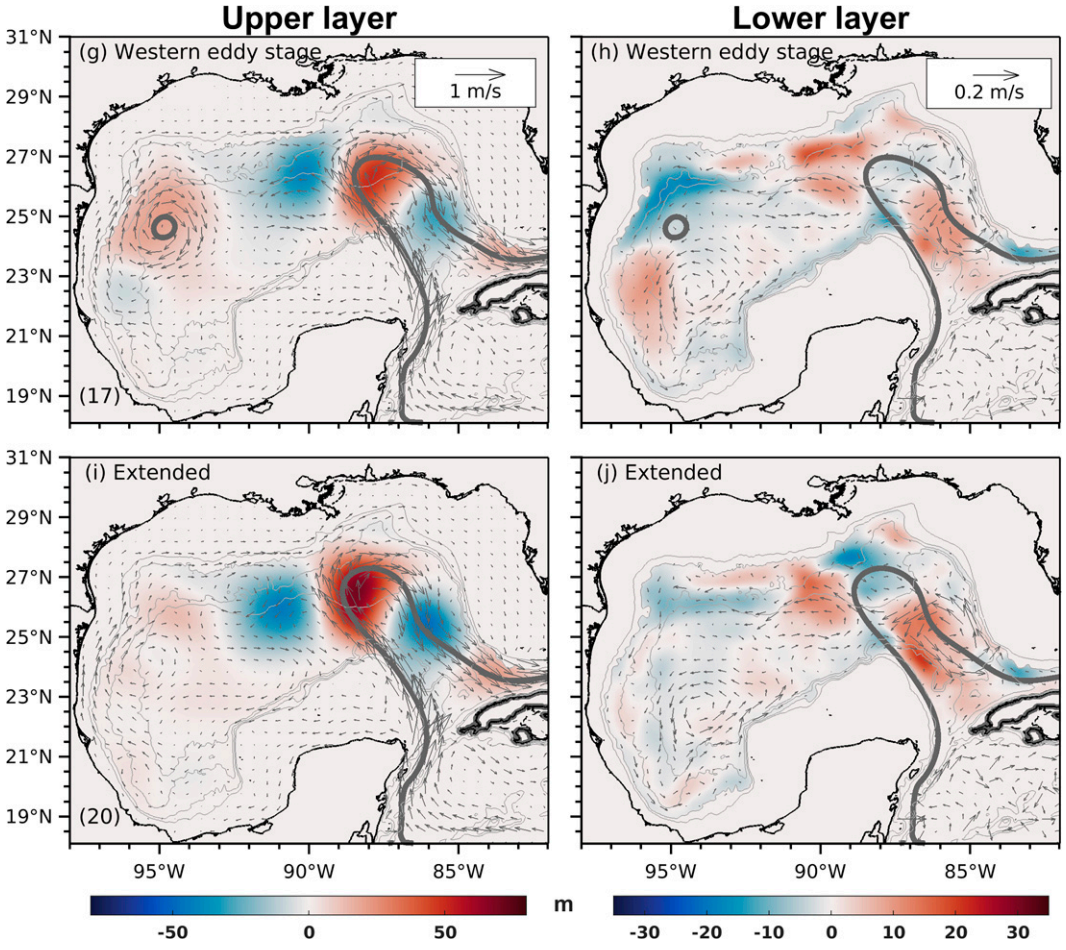

FIG. 9. Composites of reconstructed (left) upper- and (right) lower-layer thickness anomalies for different LC and LCE stages, considering the four leading modes: western eddy (LCE at ~95°W) and extended stage. The corresponding composites of model velocity (vectors) and 17-cm SSH contour (thick gray contour) in each stage are also shown. The number of events used to make the composites is indicated in the lower left corner for each stage.

(2018). Therefore, the LCE translation, the lower-layer anomalies along the boundary, the modon in the lower layer, and the cyclonic circulation in the abyssal plain are closely related. Finally, in the LC extended stage composite (Fig. 9j) after the LCE dissipates, it is observed that in the lower layer the SAG structure and circulation shows similar strength.

The composite analysis of the propagation of the upper–lower coupled variability carried out in this study contributes to corroborating the recurrent character of the LCE separation process documented for three eddy detachments in the observational study by Donohue et al. (2016b); and the description of the large-scale circulation of the lower layer reported in the observational studies of Pérez-Brunius et al. (2018) and Furey et al. (2018), particularly the semipermanent nature of the Sigsbee Abyssal Gyre.

4. Conclusions

From a HEOF analysis of a long-term numerical simulation, we have addressed an in-depth analysis of the coupling between the upper- and lower-layer variability. We have learned that in the eastern GoM, the LC life cycle and the LCE separation process in the upper layer (<250 m) is strongly related to the lower-layer (>1000 m) variability, intensified following certain steep bathymetric features. We showed that specific lower-layer patterns, previously regarded as mean features in the deep GoM, are consistently tied to the upper-layer dynamics, for example, the cyclone and a cyclone–anticyclone dipole below the LC is in fact a recurrent and dominant feature with a periodicity that agrees with the mean LCE separation period. In the western GoM, the upper variability is dominated by the traveling of LCEs west of 92°W and their arrival and dissipation in the northwestern basin. The associated lower layer variability is able to capture the convergence and divergence of water along the northwest and west boundary of the basin, and the strengthening of the circulation along the Sigsbee Gyre western branch. The results of this study add evidence and are consistent with recent observational studies.

Several efforts are underway to implement methodologies for ocean data assimilation systems in the full water column. Examples of these methods include deep ocean streamfunction

reconstruction from synthetic SSH observations using a machine learning approach (Manucharyan et al. 2021; Sonnewald et al. 2021), and reconstruction of deep ocean currents from surface velocities, SSH, and surface temperature derived from satellite observations using iterative self-organizing maps (Chapman and Charantonis 2017). We propose that the application of the HEOF technique used in this study can complement the three-dimensional oceanic assimilation methods by projecting information from surface fields to depth fields in a statistically consistent manner.

In the analysis, dominant modes of coupled variability in the southern GoM were not found. A possible explanation for this can be associated with the approach used to obtain the coupled variability modes. It is well known that the variability of the Campeche Gyre in the western Bay of Campeche is weaker than in the northern and eastern GoM (Vázquez de la Cerda et al. 2005). Thus, the modes describing its variability probably were relegated to lower modes, which were not analyzed in this study. Alternative numerical approaches to estimate the variability in the Bay of Campeche throughout the water column and to partition the processes governing its dynamics should be explored. Such studies are underway.

Acknowledgments. This study is a contribution of the Consorcio de Investigación del Golfo de México (CIGoM) through the project 201441 "Implementación de redes de observación oceanográficas (físicas, geoquímicas, ecológicas) para la generación de escenarios ante posibles contingencias relacionadas a la exploración y producción de hidrocarburos en aguas profundas del Golfo de México" funded by Secretary of Energy (SENER)-National Council of Science and Technology of Mexico (CONACyT) Hydrocarbons Fund, through a postdoctoral grant awarded to Erick Olvera. The first author also thanks the program of postdoctoral fellowships UNAM-DGAPA. The authors acknowledge the support obtained through the project UNAM-PAPIIT IA104320, as well as the Instituto de Ciencias de la Atmósfera y Cambio Climático of the Universidad Nacional Autónoma de México for the use of the cluster Ometeotl. We thank the editor, Dr. Joseph LaCasce, and the two anonymous reviewers for valuable contributions to the manuscript.

Data availability statement. Data files are archived in a Zenodo repository (https://doi.org/10.5281/zenodo.5605092).

APPENDIX

The Hilbert Empirical Orthogonal Functions

In the Hilbert empirical orthogonal function (Hilbert EOF) analysis, the state and tendency of a system are described by combining the original vector time series $\mathbf{X}(t)$ with its Hilbert transform $\mathbf{X}^H(t)$ in a new vector (von Storch and Zwiers 1999):

$$\mathbf{Y}(t) = \mathbf{X}(t) + i\mathbf{X}^H(t), \tag{A1}$$

where $i = \sqrt{-1}$ and t denotes the temporal dimension. If the variability of a time series is confined to a relatively narrow time scale, its Hilbert transform is identical to the original one but $\pi/2$ phase-shifted (a quarter of period to the right), and it can be interpreted as the time derivative or a time rate of change of the original time series (Horel 1984; von Storch and Zwiers 1999). The vector $\mathbf{Y}(t)$ represents the complexified vector time series of $\mathbf{X}(t)$, which is analyzed using the conventional EOF technique (von Storch and Zwiers 1999):

$$\mathbf{Y}(t) = \sum_k \alpha_k(t)\boldsymbol{\phi}^k = \sum_k \mathbf{Y}^k(t), \tag{A2}$$

$$\Re\mathbf{Y}(t) = \Re\alpha_k(t)\boldsymbol{\phi}^k, \tag{A3}$$

with

$$\mathbf{X}(t) = \sum_k \Re\mathbf{Y}^k(t), \quad \text{and} \quad \mathbf{X}^H(t) = \sum_k \Im\mathbf{Y}^k(t), \tag{A4}$$

where k runs over the dimension of the vector $\mathbf{Y}(t)$, $\boldsymbol{\phi}(t)$ are the Hilbert EOFs, $\alpha_k(t)$ are the EOF coefficients (or the principal components), and letters $\Re$ and $\Im$ indicate the real and imaginary parts. The original vector time series and its Hilbert transform have the same Hilbert EOF expansion, with equal amounts of variance (von Storch and Zwiers 1999).

The EOFs and their coefficients are complex, so they can be displayed using polar coordinates in terms of their amplitude and phase,

$$\boldsymbol{\phi}^k = \mathbf{A}^k \exp i\boldsymbol{\theta}^k, \tag{A5}$$

$$\alpha_k(t) = a_k(t)\exp i\psi_k(t), \tag{A6}$$

or using Cartesian coordinates in terms of their real and imaginary components,

$$\boldsymbol{\phi}^k = \boldsymbol{\phi}^k_R + i\boldsymbol{\phi}^k_I, \tag{A7}$$

$$\alpha_k(t) = a_k(t)\cos[\psi_k(t)] + ia_k(t)\sin[\psi_k(t)], \tag{A8}$$

where $\mathbf{A}^k$ and $\boldsymbol{\theta}^k$ are the amplitude and phase of the EOF $\boldsymbol{\phi}^k$, respectively; $a_k(t)$ and $\psi_k(t)$ are the amplitude and phase of the EOF coefficient $\alpha_k(t)$, respectively; and $\boldsymbol{\phi}^k_R$ and $\boldsymbol{\phi}^k_I$ are the real and imaginary components of $\boldsymbol{\phi}^k$, respectively. Thus, the representation of the vector $\mathbf{Y}(t)$ by the kth EOF at time t can be expressed as the rotation of such EOF through an angle $\psi_k(t)$ and scaled by a factor $a_k(t)$ (von Storch and Zwiers 1999):

$$\mathbf{Y}^k(t) = a_k(t)\mathbf{A}^k \exp i[\boldsymbol{\theta}^k + \psi_k(t)], \tag{A9}$$

$$\Re\mathbf{Y}^k(t) = a_k(t)\{\cos[\psi_k(t)]\boldsymbol{\phi}^k_R - \sin[\psi_k(t)]\boldsymbol{\phi}^k_I\}, \tag{A10}$$

$$\Im\mathbf{Y}^k(t) = a_k(t)\{\sin[\psi_k(t)]\boldsymbol{\phi}^k_R + \cos[\psi_k(t)]\boldsymbol{\phi}^k_I\}, \tag{A11}$$

where $\Re\mathbf{Y}^k(t)$ represents the reconstructed field using EOF k. For a specific Hilbert EOF, if the phase of the EOF coefficient covers a complete cycle in a monotonic fashion, it can be inferred to have cyclical behavior in the original data. Table A1 shows the typical temporal evolution of the vector $\mathbf{Y}^k(t)$.

TABLE A1. Temporal evolution of the vector $\mathbf{Y}^k(t)$ for some values of the phase $\psi_k(t)$ of the EOF coefficient. The amplitude of the EOF coefficient is $a_k(t)$, and $\boldsymbol{\phi}_R^k$ and $\boldsymbol{\phi}_I^k$ are the real and imaginary components of the Hilbert EOF, respectively.

$\psi_k(t)$	$\Re\mathbf{Y}^k(t)$	$\Im\mathbf{Y}^k(t)$
0	$a_k(t)\boldsymbol{\phi}_R^k$	$a_k(t)\boldsymbol{\phi}_I^k$
$-\pi/4$	$a_k(t)/\sqrt{2}(\boldsymbol{\phi}_R^k + \boldsymbol{\phi}_I^k)$	$a_k(t)/\sqrt{2}(-\boldsymbol{\phi}_R^k + \boldsymbol{\phi}_I^k)$
$-\pi/\pi 2$	$a_k(t)\boldsymbol{\phi}_I^k$	$-a_k(t)\boldsymbol{\phi}_R^k$
$-3\pi/4$	$a_k(t)/\sqrt{2}(-\boldsymbol{\phi}_R^k + \boldsymbol{\phi}_I^k)$	$a_k(t)/\sqrt{2}(-\boldsymbol{\phi}_R^k - \boldsymbol{\phi}_I^k)$
$\pm\pi$	$-a_k(t)\boldsymbol{\phi}_R^k$	$-a_k(t)\boldsymbol{\phi}_I^k$
$3\pi/4$	$a_k(t)/\sqrt{2}(-\boldsymbol{\phi}_R^k - \boldsymbol{\phi}_I^k)$	$a_k(t)/\sqrt{2}(\boldsymbol{\phi}_R^k - \boldsymbol{\phi}_I^k)$
$\pi/2$	$-a_k(t)\boldsymbol{\phi}_I^k$	$a_k(t)\boldsymbol{\phi}_R^k$
$\pi/4$	$a_k(t)/\sqrt{2}(\boldsymbol{\phi}_R^k - \boldsymbol{\phi}_I^k)$	$a_k(t)/\sqrt{2}(\boldsymbol{\phi}_R^k + \boldsymbol{\phi}_I^k)$

In the computation of the vector $\mathbf{Y}(t)$ it is assumed that the mean, trend, climatology, and any other signal have been removed from the data vector $\mathbf{X}(t)$. The Hilbert EOF analysis comprises the estimation of the EOFs $\boldsymbol{\phi}^k$ and their coefficients $\alpha_k(t)$, which can be carried out through the eigenvalue problem of the covariance matrix of the vector $\mathbf{Y}(t)$ using canned computer software (von Storch and Zwiers 1999).

The *proportion of explained variance* is the percentage of the total variance that is explained by a particular mode:

$$\eta = 1 - \frac{\mathrm{Var}(P - F)}{\mathrm{Var}(P)} \tag{A12}$$

where P is the original data and F is the reconstruction using a particular mode.

REFERENCES

Athié, G., J. Sheinbaum, R. Leben, J. Ochoa, M. R. Shannon, and J. Candela, 2015: Interannual variability in the Yucatan Channel Flow. *Geophys. Res. Lett.*, **42**, 1496–1503, https://doi.org/10.1002/2014GL062674.

Bunge, L., J. Ochoa, A. Badan, J. Candela, and J. Sheinbaum, 2002: Deep flows in the Yucatan Channel and their relation to changes in the Loop Current Extension. *J. Geophys. Res.*, **107**, 26-1–26-7, https://doi.org/10.1029/2001JC001256.

Chang, Y.-L., and L.-Y. Oey, 2011: Loop Current cycle: Coupled response of the Loop Current with deep flows. *J. Phys. Oceanogr.*, **41**, 458–471, https://doi.org/10.1175/2010JPO4479.1.

——, and ——, 2013: Loop Current growth and eddy shedding using models and observations: Numerical process experiments and satellite altimetry data. *J. Phys. Oceanogr.*, **43**, 669–689, https://doi.org/10.1175/JPO-D-12-0139.1.

Chapman, C., and A. A. Charantonis, 2017: Reconstruction of subsurface velocities from satellite observations using iterative self-organizing maps. *IEEE Geosci. Remote Sens. Lett.*, **14**, 617–620, https://doi.org/10.1109/LGRS.2017.2665603.

Chassignet, E. P., and Coauthors, 2006: Generalized vertical coordinates for eddy-resolving global and coastal ocean forecasts. *Oceanography*, **19**, 118–129, https://doi.org/10.5670/oceanog.2006.95.

Chérubin, L. M., W. Sturges, and E. P. Chassignet, 2005: Deep flow variability in the vicinity of the Yucatan Straits from a high-resolution numerical simulation. *J. Geophys. Res.*, **110**, C04009, https://doi.org/10.1029/2004JC002280.

Cromwell, D., 2006: Temporal and spatial characteristics of sea surface height variability in the North Atlantic Ocean. *Ocean Sci.*, **2**, 147–159, https://doi.org/10.5194/os-2-147-2006.

Donohue, K. A., P. Hamilton, R. Leben, R. Watts, and E. Waddell, 2008: Survey of deepwater currents in the northwestern Gulf of Mexico, volume 2. Tech. Rep. MMS Tech. Rep. MMS 2008-031, 91 pp.

——, D. R. Watts, P. Hamilton, R. R. Leben, M. A. Kennelly, and A. Lugo-Fernandez, 2016a: Gulf of Mexico Loop Current path variability. *Dyn. Atmos. Oceans*, **76**, 174–194, https://doi.org/10.1016/j.dynatmoce.2015.12.003.

——, ——, ——, ——, and ——, 2016b: Loop Current eddy formation and baroclinic instability. *Dyn. Atmos. Oceans*, **76**, 195–216, https://doi.org/10.1016/j.dynatmoce.2016.01.004.

Dukhovskoy, D. S., S. L. Morey, P. J. Martin, J. J. O'Brien, and C. Cooper, 2009: Application of a vanishing, quasi-sigma, vertical coordinate for simulation of high-speed, deep currents over the Sigsbee Escarpment in the Gulf of Mexico. *Ocean Modell.*, **28**, 250–265, https://doi.org/10.1016/j.ocemod.2009.02.009.

——, R. R. Leben, E. P. Chassignet, C. A. Hall, S. L. Morey, and R. Nedbor-Gross, 2015: Characterization of the uncertainty of Loop Current metrics using a multidecadal numerical simulation and altimeter observations. *Deep-Sea Res. I*, **100**, 140–158, https://doi.org/10.1016/j.dsr.2015.01.005.

Furey, H., A. Bower, P. Perez-Brunius, P. Hamilton, and R. Leben, 2018: Deep eddies in the Gulf of Mexico observed with floats. *J. Phys. Oceanogr.*, **48**, 2703–2719, https://doi.org/10.1175/JPO-D-17-0245.1.

Hall, C. A., and R. R. Leben, 2016: Observational evidence of seasonality in the timing of Loop Current eddy separation. *Dyn. Atmos. Oceans*, **76**, 240–267, https://doi.org/10.1016/j.dynatmoce.2016.06.002.

Hamilton, P., 1990: Deep currents in the Gulf of Mexico. *J. Phys. Oceanogr.*, **20**, 1087–1104, https://doi.org/10.1175/1520-0485(1990)020<1087:DCITGO>2.0.CO;2.

——, 2007: Deep-current variability near the Sigsbee Escarpment in the Gulf of Mexico. *J. Phys. Oceanogr.*, **37**, 708–726, https://doi.org/10.1175/JPO2998.1.

——, 2009: Topographic Rossby waves in the Gulf of Mexico. *Prog. Oceanogr.*, **82** (1), 1–31, https://doi.org/10.1016/j.pocean.2009.04.019.

——, and A. Lugo-Fernandez, 2001: Observations of high speed deep currents in the northern Gulf of Mexico. *Geophys. Res. Lett.*, **28**, 2867–2870, https://doi.org/10.1029/2001GL013039.

——, ——, and J. Sheinbaum, 2016: A Loop Current experiment: Field and remote measurements. *Dyn. Atmos. Oceans*, **76**, 156–173, https://doi.org/10.1016/j.dynatmoce.2016.01.005.

——, R. Leben, A. Bower, H. Furey, and P. Pérez-Brunius, 2018: Hydrography of the Gulf of Mexico using autonomous floats. *J. Phys. Oceanogr.*, **48**, 773–794, https://doi.org/10.1175/JPO-D-17-0205.1.

——, A. Bower, H. Furey, R. Leben, and P. Pérez-Brunius, 2019: The Loop Current: Observations of deep eddies and topographic waves. *J. Phys. Oceanogr.*, **49**, 1463–1483, https://doi.org/10.1175/JPO-D-18-0213.1.

Horel, J. D., 1984: Complex principal component analysis: Theory and examples. *J. Climate Appl. Meteor.*, **23**, 1660–1673,

https://doi.org/10.1175/1520-0450(1984)023<1660:CPCATA>2.0.CO;2.

Leben, R. R., 2005: Altimeter-derived Loop Current metrics. *Circulation in the Gulf of Mexico: Observations and Models. Geophys. Monogr.*, Vol. 161, Amer. Geophys. Union, 181–201, https://doi.org/10.1029/161GM15.

Lee, H.-C., and G. L. Mellor, 2003: Numerical simulation of the Gulf Stream system: The Loop Current and the deep circulation. *J. Geophys. Res.*, **108**, 3043, https://doi.org/10.1029/2001JC001074.

Liu, Y., R. H. Weisberg, S. Vignudelli, and G. T. Mitchum, 2016: Patterns of the Loop Current system and regions of sea surface height variability in the eastern Gulf of Mexico revealed by the self-organizing maps. *J. Geophys. Res. Oceans*, **121**, 2347–2366, https://doi.org/10.1002/2015JC011493.

Manucharyan, G. E., L. Siegelman, and P. Klein, 2021: A deep learning approach to spatiotemporal sea surface height interpolation and estimation of deep currents in geostrophic ocean turbulence. *J. Adv. Model. Earth Syst.*, **13**, e2019MS001965, https://doi.org/10.1029/2019MS001965.

Maslo, A., J. Sheinbaum, and J. M. Azevedo Correia de Souza, 2020: Energetics of the deep Gulf of Mexico. *J. Phys. Oceanogr.*, **50**, 1655–1675, https://doi.org/10.1175/JPO-D-19-0308.1.

Meza-Padilla, R., C. Enriquez, Y. Liu, and C. M. Appendini, 2019: Ocean circulation in the western Gulf of Mexico using self-organizing maps. *J. Geophys. Res. Oceans*, **124**, 4152–4167, https://doi.org/10.1029/2018JC014377.

Morey, S. L., and D. S. Dukhovskoy, 2013: A downscaling method for simulating deep current interactions with topography—Application to the Sigsbee Escarpment. *Ocean Modell.*, **69**, 50–63, https://doi.org/10.1016/j.ocemod.2013.05.008.

——, and Coauthors, 2020: Assessment of numerical simulations of deep circulation and variability in the Gulf of Mexico using recent observations. *J. Phys. Oceanogr.*, **50**, 1045–1064, https://doi.org/10.1175/JPO-D-19-0137.1.

Nedbor-Gross, R., D. S. Dukhovskoy, M. A. Bourassa, S. L. Morey, and E. P. Chassignet, 2014: Investigation of the relationship between the Yucatan Channel transport and the Loop Current area in a multidecadal numerical simulation. *Mar. Technol. Soc. J.*, **48**, 15–26, https://doi.org/10.4031/MTSJ.48.4.8.

North, G. R., T. L. Bell, R. F. Cahalan, and F. J. Moeng, 1982: Sampling errors in the estimation of empirical orthogonal functions. *Mon. Wea. Rev.*, **110**, 699–706, https://doi.org/10.1175/1520-0493(1982)110<0699:SEITEO>2.0.CO;2.

Oey, L.-Y., 2008: Loop Current and deep eddies. *J. Phys. Oceanogr.*, **38**, 1426–1449, https://doi.org/10.1175/2007JPO3818.1.

Pérez-Brunius, P., H. Furey, A. Bower, P. Hamilton, J. Candela, P. García-Carrillo, and R. Leben, 2018: Dominant circulation patterns of the deep Gulf of Mexico. *J. Phys. Oceanogr.*, **48**, 511–529, https://doi.org/10.1175/JPO-D-17-0140.1.

Romanou, A., E. P. Chassignet, and W. Sturges, 2004: Gulf of Mexico circulation within a high-resolution numerical simulation of the North Atlantic Ocean. *J. Geophys. Res.*, **109**, C01003, https://doi.org/10.1029/2003JC001770.

Sonnewald, M., R. Lguensat, D. Jones, P. Düben, J. Brajard, and V. Balaji, 2021: Bridging observation, theory and numerical simulation of the ocean using machine learning. *Environ. Res. Lett.*, **16**, 073008, https://doi.org/10.1088/1748-9326/ac0eb0.

Sturges, W., and R. Leben, 2000: Frequency of ring separations from the Loop Current in the Gulf of Mexico: A revised estimate. *J. Phys. Oceanogr.*, **30**, 1814–1819, https://doi.org/10.1175/1520-0485(2000)030<1814:FORSFT>2.0.CO;2.

Tenreiro, M., J. Candela, E. P. Sanz, J. Sheinbaum, and J. Ochoa, 2018: Near-surface and deep circulation coupling in the western Gulf of Mexico. *J. Phys. Oceanogr.*, **48**, 145–161, https://doi.org/10.1175/JPO-D-17-0018.1.

Vázquez de la Cerda, A. M., R. O. Reid, S. F. DiMarco, and A. E. Jochens, 2005: Bay of Campeche circulation: An update. *Circulation in the Gulf of Mexico: Observations and Models, Geophys. Monogr.*, Vol. 161, Amer. Geophys. Union, 279–293, https://doi.org/10.1029/161GM20.

von Storch, H., and F. W. Zwiers, 1999: *Statistical Analysis in Climate Research*. Cambridge University Press, 300 pp.

Vukovich, F. M., 2007: Climatology of ocean features in the Gulf of Mexico using satellite remote sensing data. *J. Phys. Oceanogr.*, **37**, 689–707, https://doi.org/10.1175/JPO2989.1.

——, 2012: Changes in the Loop Current's eddy shedding in the period 2001–2010. *Int. J. Oceanogr.*, **2012**, 11–18, https://doi.org/10.1155/2012/439042.

Welsh, S. E., and M. Inoue, 2000: Loop Current rings and the deep circulation in the Gulf of Mexico. *J. Geophys. Res.*, **105**, 16 951–16 959, https://doi.org/10.1029/2000JC900054.

Yang, Y., R. H. Weisberg, Y. Liu, and X. San Liang, 2020: Instabilities and multiscale interactions underlying the Loop Current eddy shedding in the Gulf of Mexico. *J. Phys. Oceanogr.*, **50**, 1289–1317, https://doi.org/10.1175/JPO-D-19-0202.1.

Zavala-Hidalgo, J., S. Morey, and J. O'Brien, 2003: Cyclonic eddies northeast of the Campeche Bank from altimetry data. *J. Phys. Oceanogr.*, **33**, 623–629, https://doi.org/10.1175/1520-0485(2003)033<0623:CENOTC>2.0.CO;2.

——, ——, ——, and L. Zamudio, 2006: On the Loop Current eddy shedding variability. *Atmósfera*, **19**, 41–48, https://www.revistascca.unam.mx/atm/index.php/atm/article/view/8551.

Zeng, X., Y. Li, and R. He, 2015: Predictability of the Loop Current variation and eddy shedding process in the Gulf of Mexico using an artificial neural network approach. *J. Atmos. Oceanic Technol.*, **32**, 1098–1111, https://doi.org/10.1175/JTECH-D-14-00176.1.